Regression Algorithm Correcting for Partial Volume Effects in Arterial Spin Labeling MRI

Iris Asllani,[1*] Ajna Borogovac,[2] and Truman R. Brown[1,2]

Partial volume effects (PVE) are a consequence of limited spatial resolution in brain imaging. In arterial spin labeling (ASL) MRI, the problem is exacerbated by the nonlinear dependency of the ASL signal on magnetization contributions from each tissue within an imaged voxel. We have developed an algorithm that corrects for PVE in ASL imaging. The algorithm is based on a model that represents the voxel intensity as a weighted sum of pure tissue contribution, where the weighting coefficients are the tissue's fractional volume in the voxel. Using this algorithm, we were able to estimate cerebral blood flow (CBF) for gray matter (GM) and white matter (WM) independently. The average voxelwise ratio of GM to WM CBF was ~3.2, in good agreement with reports in the literature. As proof of concept, data from PVE-corrected method were compared with those from the conventional, PVE-uncorrected method. As hypothesized, the two yielded similar CBF values for voxels containing >95% GM and differed in proportion with the voxels' heterogeneity. More importantly, the GM CBF assessed with the PVE-corrected method was independent of the voxels' heterogeneity, implying that estimation of flow was unaffected by PVE. An example of application of this algorithm in motor-activation data is also given. Magn Reson Med 60:1362–1371, 2008.

Key words: ASL; CBF; linear regression; MRI; partial volume effects; perfusion

Arterial spin labeling (ASL) is a noninvasive MRI method that provides a direct and quantifiable measurement of cerebral blood flow (CBF). Conceptually, ASL is similar to positron emission tomography (PET) and as such, the results from ASL are often compared with those from H_2O^{15} PET (1,2). However, both methods are significantly affected by partial volume effects (PVE) caused by two main mechanisms: 1) blurring due to the point spread function (PSF), and 2) mixing of tissue-specific signals (i.e., signal cross-contamination) due to voxel heterogeneity. Although several algorithms have been developed to address PVE in PET (3–5), only one has attempted to correct the effects of signal cross-contamination by including local tissue fractions (6). So far, no such algorithm has been developed for ASL, where PVE due to signal cross-contamination are particularly troublesome because the measured signal is a ratio of two images, each of which is affected by voxel heterogeneity.

ASL measurement is based on the difference between a labeled and a control image (7). In continuous ASL (CASL), the labeled image is acquired with the flowing arterial spins being magnetically altered via inversion in order to distinguish them from the static tissue spins; the control image is acquired with all the spins being in the same magnetic state. At a given voxel, the difference between the control and labeled images is proportional to the amount of flow and is commonly expressed as a fractional signal change, $\left(\frac{M_C - M_L}{M_C}\right)$ where M_C and M_L represent the control and label magnetizations, respectively. Because control/label pairs need to be acquired consecutively and rapidly, fast imaging methods such as EPI are commonly employed at the expense of spatial resolution. Thus, the measured ASL signal from a given voxel typically includes contributions from all three tissues—gray matter (GM), white matter (WM), and cerebral spinal fluid (CSF)— as:

$$\left(\frac{\Delta M}{M_C}\right) = \frac{(P_{GM}\cdot \Delta M_{GM}) + (P_{WM}\cdot \Delta M_{WM}) + (P_{CSF}\cdot \Delta M_{CSF})}{(P_{GM}\cdot M_{GM} + P_{WM}\cdot M_{WM} + P_{CSF}\cdot M_{CSF})} \quad [1]$$

where $\frac{\Delta M}{M_C}$ denotes the ASL fractional signal change and represents the raw signal in a typical ASL experiment; and P, M, and ΔM denote the fractional tissue volume, the control EPI magnetization, and the difference between control and label magnetization, respectively, with the subscript denoting tissue type. Typically, ΔM_{CSF} is assumed to be zero (8,9). Each label/control pair is subsequently transformed to a single CBF image using a physical model and a set of measured or assumed MR parameters such as tissue and arterial T_1, etc. (10).

In most disease and/or functional studies, the tissue of interest is GM. Generally, a trichotomized approach assigns a voxel to a tissue type; if a voxel falls within an a priori tissue classification criterion, that voxel is deemed to be made entirely of that tissue. Often, posterior probability masks are obtained from high-resolution MRI and a voxel is considered GM if its $P[GM]$ is larger than a threshold value, commonly chosen to be 0.8 (9,11) or 0.7 (12). Alternatively, T_1 images are acquired and a given voxel is deemed GM if its T_1 value falls within the a priori chosen range (13). There are no studies, however, in which corrections for PVE were made to either the numerator or denominator of Eq. [1].

PVE can be quite appreciable in cortical regions where GM can be as thin as 2 mm (5). To give a sense of the magnitude of these effects, a voxel containing 80% GM and 20% CSF would, under the above criteria, be assumed and analyzed as a GM voxel. For such a voxel, a simple calculation (Eq. [1]) assuming the relative tissue magneti-

[1]Department of Radiology, College of Physicians and Surgeons, Columbia University, New York, New York, USA.

[2]Department of Biomedical Engineering, College of Physicians and Surgeons, Columbia University, New York, New York, USA.

*Correspondence to: Dr. Iris Asllani, Hatch Center for MR Research, Columbia University, 710 W. 168th St., New York, NY 10032. E-mail: ia2026@columbia.edu

Received 13 November 2007; revised 19 March 2008; accepted 31 March 2008.

DOI 10.1002/mrm.21670

Published online 30 September 2008 in Wiley InterScience (www.interscience.wiley.com).

zation intensities for SE-EPI to be $M_{CSF} : M_{GM} : M_{WM} \sim 1.6:1.2:1.0$ (14), would underestimate its GM CBF by ~24 %.

Here we present an algorithm that corrects for PVE due to tissue cross-contamination in ASL. The algorithm is based on linear regression and estimates the *pure* tissue signals by modeling the SE-EPI intensity of a given voxel as a weighted sum of m_{GM}, m_{WM}, and m_{CSF} contributions, whereas the ASL difference signal (ΔM) is expressed as a weighted sum of δm_{GM}, δm_{WM}, and δm_{CSF} tissue contributions. The weighting coefficients in both cases are the tissue's fractional volumes obtained as posterior probability values from segmentation of high-resolution images.

MATERIALS AND METHODS

Theory

In current ASL methods, a fractional signal change image, $\left(\frac{\Delta M}{M_C}\right)$, is typically converted to a CBF image, f, as:

$$f_{tissue} = \left(\frac{\Delta M}{M_C}\right) \cdot F_{tissue} \quad [2]$$

where F_{tissue} takes into account tissue-specific parameters such as T_1 and the blood–brain partition coefficient, as well as acquisition parameters such as the postlabeling delay (7).

Given the limited spatial resolution of ASL, the $\left(\frac{\Delta M}{M_C}\right)$ term contains contributions from GM, WM, and CSF. Ideally, we want to be able to separate these contributions and compute CBF independently for "partial" GM and "partial" WM flow as:

$$f^p_{GM} = P_{GM} \cdot \left(\frac{\delta m_{GM}}{m_{GM}}\right) \cdot F_{GM} \quad [3]$$

$$f^p_{WM} = P_{WM} \cdot \left(\frac{\delta m_{WM}}{m_{WM}}\right) \cdot F_{WM} \quad [4]$$

and compute the net CBF as a sum of these partial contributions:

$$f_{NET} = f^p_{GM} + f^p_{WM} \quad [5]$$

To achieve this, five parameters—m_{GM}, m_{WM}, m_{CSF}, Δm_{GM}, and Δm_{WM}—need to be separately estimated at each voxel. For a single voxel this is not possible because we have only two equations to estimate five parameters. However, by assuming that in the local region around each voxel these parameters remain constant, we can now bring more equations to bear. The algorithm presented here makes such assumption and uses linear regression to model M_C and ΔM as weighted sums of pure tissue contributions, with the weighting coefficient being the fractional volumes of each tissue type.

The regression analysis is run in two steps. The first step estimates m_{GM}, m_{WM}, m_{CSF} from the control EPI image, while the second estimates Δm_{GM} and Δm_{WM} from the difference image (assuming $\Delta m_{CSF} = 0$). Each step corrects for PVE in the denominator and numerator of Eq. [2], respectively, with the combined result being a tissue-specific ASL signal.

Step 1. For each voxel at position r_i, its intensity, $M(r_i)$, from the EPI control image is expressed as a weighted sum of individual contributions from GM, WM, and CSF as:

$$M(r_i) = P_j(r_i) \cdot m_j(r_i) \quad [6]$$

where $P_j(r_i)$ is a row vector of the tissue type fractions at r_i, and $m_j(r_i)$, which we seek to estimate, is a column vector of the intensities of the j^{th} tissue type at r_i. (For this study, $P_j(r_i)$ were obtained from the segmentation of high-resolution spoiled gradient [SPGR] images using SPM99 software from the Wellcome Department of Cognitive Neurology).

By assuming $m_j(r_i) = \bar{m}_j$ over a $(n^2 \times 1)$ regression-kernel centered at voxel r_i, we can estimate $\bar{m}_j$ using linear regression analysis as:

$$\bar{M}(r_k) = P_{kj} \cdot \bar{m}_j \quad [7]$$

where $\bar{M}(r_k)$ is the column vector of the n^2 values of the observed magnetization at each voxel in the regression-kernel, P_{kj} is the $(n^2 \times 3)$ matrix formed by stacking the individual $P_j(r_k)$'s from each voxel in the regression-kernel, and m_j is the column vector of local tissue type magnetizations.

The standard least-squares solution to Eq. [7] gives the following:

$$\bar{m} = (P^T \cdot P)^{-1} \cdot P^T \cdot \bar{M} \quad [8]$$

where $(P^T \cdot P)^{-1} \cdot P^T$ is the $(3 \times n^2)$ pseudo-inverse of matrix P (15).

Step 2. The analysis in this step uses the difference images, ΔM. Here, for each voxel at position r_i, the intensity of the ΔM image is expressed as a weighted sum of individual pure tissue contributions:

$$\Delta M(r_i) = P_j(r_i) \cdot \delta m(r_i) \quad [9]$$

Assuming $\delta m(r_i) = \delta \bar{m}_j$ over the regression-kernel, $\delta \bar{m}_j$ is then again estimated as:

$$\delta \bar{m} = (P^T \cdot P)^{-1} \cdot P^T \cdot \Delta \bar{M} \quad [10]$$

In both steps, there is an inherent degree of spatial "blurring" resulting from the assumptions that tissue magnetization (step 1) and perfusion (step 2) are constant over the kernel area. However, the kernel is not a smoothing filter in the conventional sense (i.e., it does not simply average the data over the region), which is why we refer to its blurring effect as "smoothing" in quotation marks, and to the kernel itself as the regression-kernel throughout this work.

Image Acquisition

Subjects

CASL perfusion images were acquired on seven healthy volunteers (two males and five females, age = 27 ± 5 years) under the protocol described below. Written consent was obtained from all subjects as approved by the Columbia University IRB.

MRI Acquisition

For each subject, 30 CASL SE-EPI labeled/control pairs and a high-resolution T_1-weighted, 3D SPGR sequence were acquired on a 1.5 T Philips Intera scanner. CASL images were acquired as described in Ref. 11. Briefly, the acquisition parameters were: labeling duration = 2000 ms, postlabeling delay (PLD) = 800 ms, TE/TR = 35 ms/5000 ms, flip angle = 90°, FOV = 220 × 192.5 mm^2, in-plane resolution = 3.4 × 3.4 mm^2, slice thickness/gap = 8.0 mm/1.0 mm, number of axial slices = 15. Slices were acquired in ascending mode with slice acquisition time = 64 ms.

SPGR was acquired with: TE/TR = 3 ms/34 ms, flip angle = 45°, acquisition matrix = 256 × 256 × 124, voxel size = 0.94 × 0.94 × 1.29 mm^3.

Image Processing and Data Analysis

Preprocessing

Preprocessing was implemented using SPM99 software and other in-house code written in MATLAB (The MathWorks, Natick, MA, USA). For each subject, images were preprocessed as follows: 1) all EPI images were realigned to the first acquired; 2) GM, WM, and CSF posterior probability images were obtained from the SPGR using SPM99 segmentation algorithm; 3) the SPGR and posterior probability maps were coregistered to the first acquired EPI using the mutual information coregistration algorithm (this step effectively downsamples the SPGR to the spatial resolution of the EPI images); and 4) to remove any signal from nonbrain tissue, for each subject a mask was made by summing subject's tissue posterior probability images; only voxels within this mask (i.e., voxels having brain tissue contributions) were included in the analysis.

Segmentation of SPGR

SPM99 was used to segment the SPGR of each subject into GM, WM, and CSF posterior probability images. We use posterior probability images as a measure of relative tissue volume because the expected value of CBF for a voxel with a given $P[GM]$, $P[WM]$, and P[CSF] is that of a voxel with those relative tissue volumes. For each subject, the segmentation procedure was done in the subject's native space and then transformed into the Talairach space as described above.

Regression Analysis

For each subject, linear regression was performed in the subject's native space using regression-kernel sizes of 5 × 5 × 1, 7 × 7 × 1, 9 × 9 × 1,11 × 11 × 1, and 15 × 15 × 1. At the edge of the brain, the regression-kernel included only voxels within the analysis mask; if less than 3 voxels were available, that center voxel was set to zero. Furthermore, because the analysis relies on $(P^TP)^{-1}$ being nonsingular, any time that condition was found (i.e., when no more than 3 voxels had $P_j > 0$ for all j), that center voxel was set to zero. (This was substantial in the 3 × 3 × 1 case, which is why these results are not reported.)

The analysis was run in two steps:

Step 1. For each subject, the algorithm was applied on all 30 individual EPI control images from which time-averaged estimates of m_{GM}, m_{WM}, and m_{CSF} were obtained. Subjectwise group averages were obtained for m_{GM}, m_{WM}, and m_{CSF} images. Prior to group averaging, m_{GM} and m_{CSF} were normalized to the subject's mean m_{WM}, and results are presented as the relative mean intensities.

Step 2. For each subject, the algorithm was applied on all 30 individual difference images, δm, thus obtaining time-averaged estimates of subject's δm_{GM} and δm_{WM} that were subsequently averaged to yield subjectwise mean δm_{GM} and δm_{WM} images.

Results from both steps were used to compute fractional ASL signal images—($\delta m_{GM}/m_{GM}$) and ($\delta m_{WM}/m_{WM}$)—in each subject.

For the subsequent group analysis, all SPGR and average CBF images were transformed into the Talairach standard space and resampled to 2 × 2 × 2 mm^3 voxel size using bilinear interpolation.

To check for the effect of CSF flow, in three subjects the analysis was also run assuming $\delta m_{CSF} \neq 0$. Results were compared by looking at the difference between images acquired with and without the assumption of $\delta m_{CSF} = 0$ in the whole brain and in voxels with $P[GM] > 0.8$ and $P[WM] > 0.8$.

Estimation of Regression Errors

For each subject, the error due to regression is expressed as the square root of the mean square of errors (MSE):

$$\sqrt{MSE} = \sqrt{\frac{(\bar{M} - P \cdot m)^T \cdot (\bar{M} - P \cdot m)}{(N_{degrees\ of\ freedom})}} \qquad [11]$$

with the degrees of freedom being $(n^2 - 3)$ and $(n^2 - 2)$ for the fitting of the EPI and δm images, respectively (15).

To investigate the dependency of regression error on kernel size, average $\sqrt{MSE}$ values were computed on control EPI images for voxels with $P[GM] > 0.8$ and $P[WM] > 0.8$ for regression-kernel sizes 5 × 5 × 1, 7 × 7 × 1, 9 × 9 × 1, 11 × 11 × 1, and 15 × 15 × 1. For direct comparison of the regression error between the two tissue types, $\sqrt{MSE}$ for GM and WM were normalized to their respective mean control magnetization values.

CBF Computation

For each subject, *pure* GM and *pure* WM fractional signal images were used to compute tissue specific CBF maps as:

$$f_{GM} = \left(\frac{\delta m_{GM}}{m_{GM}}\right) \cdot F_{GM} \qquad [12]$$

$$f_{WM} = \left(\frac{\delta m_{WM}}{m_{WM}}\right) \cdot F_{WM} \quad [13]$$

where

$$F_{tissue} = \frac{\lambda}{2\alpha}\left\{ \begin{array}{l} T_{1a}\left[e^{(\min(\delta a-\omega,0)-\delta a)/T_{1a}} - e^{(\min[\delta-w,0]-\delta)/T_{1a}}\right] + \\ e^{-\delta/T_{1a}}\left[T_{1s}e^{-/T_{1ns}}(1 - e^{\min[\delta-\tau,0]/T_{1s}}) \right. \\ \left. \quad + T_1(e^{\min[\delta-\omega,0]/T_{1ns}} - e^{-[\delta/T_{1ns}}) \right. \end{array} \right\}^{-1} \quad [14]$$

in accordance with the two-compartment model (16).

Parameter notation and values were: T_1 of blood, T_{1a} = 1400 ms; blood/tissue water partition, λ = 0.95 and 0.82 ml/g for GM and WM, respectively (17); labeling duration, τ = 2000 ms; tissue T_{1ns} in the absence of saturation effects of the RF pulse, T_{1ns} = 1150 ms and 800 ms for GM and WM, respectively; T_{1s} in presence of saturation effects of the RF pulse, T_{1s} = 750 ms and 530 ms for GM and WM, respectively (7); and labeling efficiency for CASL at 1.5 T Philips Intera, α = 0.70 (18). For each slice the effective PLD, w, was adjusted to account for the slice acquisition time: w = (slice # − 1) · (64 ms) + 800 ms, as was the arterial transit time, δa (112.5 ms/slice with a starting point for the first slice of 200 ms and 420 ms for GM and WM, respectively.) This value was the average from two different studies that measured slicewise δa (11,13). Tissue transit time, δ, was assumed to vary linearly with δa with an additional exchange time assumed to be 500 ms and 700 ms for GM and WM, respectively.

From *pure* tissue CBF maps, partial GM (f^p_{GM}), partial WM (f^p_{WM}), and net CBF (f_{NET}) were computed using Eqs. [3]–[5], respectively, and were subsequently transformed into the Talairach standard space.

ROI Analysis

For each subject, five ROIs were obtained using subject's posterior probability image for GM ($P[GM]$). The $P[GM]$ image was thresholded to contain voxels with $0 < P[GM] < 0.2$, $0.2 < P[GM] < 0.4$, $0.4 < P[GM] < 0.6$, $0.6 < P[GM] < 0.8$, $0.8 < P[GM] < 1.0$. To compare the results for voxels containing mostly GM, a subset of the last ROI containing voxels with $P[GM] > 0.95$ was separately analyzed.

Activation Data

In three subjects (two males and one female, right-handed, age = 27 ± 2 years), motor-task ASL activation data were acquired from five slices positioned in the motor-cortex area of the brain. In one of the subjects, the experiment was repeated twice with a time-lag of 2 months.

The paradigm was 80 s of right-hand sequential finger tapping followed by 80 s of rest. Each Tap/Rest run was repeated five times, resulting in a total of 50 CBF images per condition. The labeling plane was positioned 100 mm inferior to the center of imaging volume. The rest of the scanning parameters were identical to the main experiment.

Data were analyzed with regression-kernels of different sizes: 5 × 5, 7 × 7, 9 × 9, 11 × 11, and 15 × 15. For comparison, they were also analyzed with the conventional, PVE-uncorrected method. To estimate the effects of "smoothing" caused by the regression-kernel, a PVE-uncorrected control EPI was spatially smoothed with a Gaussian having full-width at half-height (FWHH) varying from 3 to 15 mm (2-mm step). Ten GM voxels ($P[GM] > 0.95$) were randomly selected and their magnetization values from the smoothed PVE-uncorrected data were compared with those obtained with the smallest (5 × 5) and largest (15 × 15) regression-kernels. For each voxel and kernel size, the difference (in %) between the smoothed PVE-uncorrected data and regression estimates was computed. We report the minimum differences as averages ± standard deviation (SD).

SPM99 was used to test for voxelwise CBF differences between resting and activation states. (Because ASL CBF data lack any substantial temporal autocorrelation (19), independence of errors was assumed.) The statistical threshold was selected to control for α = 0.05 per two-tailed effect, corrected for multiple comparisons using Gaussian random field theory (20). For each case, an SPM{T} map thresholded at the respective $t_{\min}$ value for $\alpha_{corrected}$ = 0.05 was obtained. For comparison across regression-kernels and PVE-uncorrected method, a conjunction mask of all the individual SPM{T} maps was used for each subject.

RESULTS

Estimation of Tissue Magnetization and ASL Raw Signal

The first step of the algorithm estimates the magnetization contributions of each tissue type at a given voxel in the control EPI image. The histograms of the group mean m_{GM}, m_{WM}, and m_{CSF} images are shown in Fig. 1a in black, blue, and red, respectively. Maps from a randomly selected subject are shown in the inset of Fig. 1a, while maps from a randomly selected subject are shown in Fig. 1b (first, second, and third rows, respectively). From theoretical considerations, it is reasonable to expect the magnetization of each tissue type to be relatively uniform across the SE-EPI; the narrowness of the spread of the histogram for GM and WM and the uniformity of image intensities in Fig. 1b agree well with this expectation (Fig. 1). m_{CSF} was noisier, which we believe is due to arterial water and sagittal sinus being considered CSF by the analysis because of their similar magnetizations as well as a slow flow effect in the sagittal sinus.

Based on tissue T_2 values (250 ms, 95 ms, and 80 ms for CSF, GM, and WM, respectively [14]) and water content (1.0, 0.82, 0.72 for CSF, GM, and WM, respectively [14]), the theoretical magnetization ratios for SE-EPI are ~1.64 for m_{CSF}/m_{WM} and ~1.23 for m_{GM}/m_{WM}. From our data, the group mean (± SD) ratios were: m_{CSF}/m_{WM} = 1.68 ± 0.14 and m_{GM}/m_{WM} = 1.23 ± 0.03, in very good agreement with the theoretical predictions and reported experimental data acquired on a 1.5T Philips scanner (21).

The tissue fractional ASL signal images, ($\delta m_{GM}/m_{GM}$) and ($\delta m_{WM}/m_{WM}$), represent the raw ASL signal. Therefore, the value at each voxel is expected to be directly proportional to the amount of labeled spins having entered that voxel, i.e., flow. Consequently, the raw GM ASL signal is expected to be higher than that of WM (6,7). This predic-

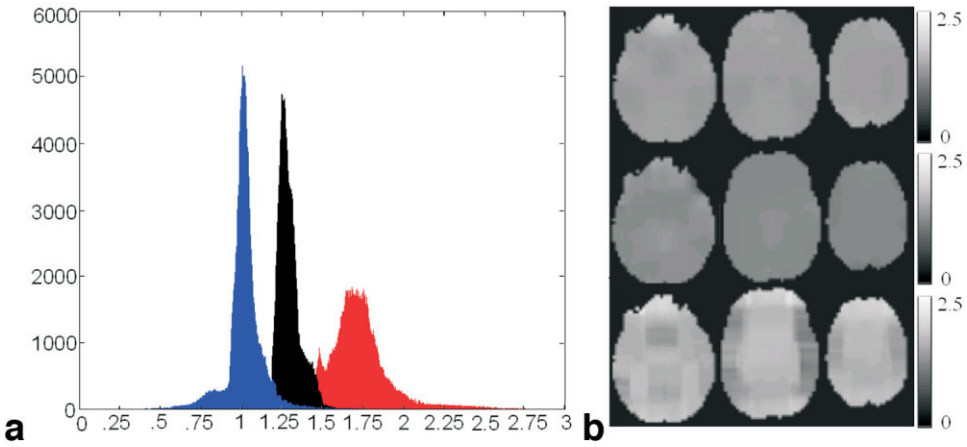

FIG. 1. **a:** Histograms of subjectwise averaged estimates of: m_{GM} (black), m_{WM} (blue), and m_{CSF} (red). For each subject, m_{GM} and m_{CSF} values were normalized to m_{WM}, respectively. **b:** Maps of m_{GM} (first row), m_{WM} (second row), and m_{CSF} (third row) from a single subject. Slices were chosen to represent the lower, middle, and upper parts of the brain. For all data, an 11 × 11 × 1 regression-kernel was used. [Color figure can be viewed in the online issue, which is available at www.interscience.wiley.com.]

tion is borne out in Fig. 2, which shows subjectwise averaged histograms for ($\delta m_{GM}/m_{GM}$) and ($\delta m_{WM}/m_{WM}$) in black and blue, respectively. The mean ratio of GM raw ASL signal to that of WM is ~3.2 (±0.5).

To give a qualitative sense of the tissue-specific raw ASL images, maps of ($\delta m_{GM}/m_{GM}$) and ($\delta m_{WM}/m_{WM}$) from a randomly selected subject are shown in Fig. 2b (first and second rows, respectively). Note the good uniformity of GM and WM flow, with GM being higher in the occipital region.

The analysis assumed $\delta m_{CSF} = 0$. To test the validity of this assumption, in three subjects the analysis was also run with $\delta m_{CSF} \neq 0$. In both cases, the effect of CSF flow on the ASL signal in GM ($P[GM] > 0.8$) and WM ($P[WM] > 0.8$) was not substantial: $\frac{\delta m_{GM}}{m_{GM}}$, expressed in percent change, went from an average of 1.02% to 0.94%, while $\frac{\delta m_{WM}}{m_{WM}}$ went from an average of 0.30 to 0.305. Over the entire brain, the effect was more pronounced (~15% difference), which we conjecture is due to large veins and sagittal sinus being considered CSF by the regression algorithm.

Regression Error and Its Dependency on Regression-Kernel Size

Group averages of the regression error, $\sqrt{MSE}$, for EPI control and ASL difference images for the 11 × 11 × 1 kernel are shown in Fig. 3, second and third rows, respectively; the corresponding SPGR slices are shown in the first row.

The dependency of $\sqrt{MSE}$ on regression-kernel size is shown in Fig. 4 for GM ($P[GM] > 0.8$) and WM ($P[WM] > 0.8$) in circles and triangles, respectively. One hypothesis for this behavior is that the larger the regression-kernel, the weaker the assumption of local uniformity, and hence the poorer the fit.

The main advantage of this method is that it yields *pure* tissue CBF maps, i.e., for any given voxel one can separately obtain a *pure* GM CBF (f_{GM}) and a *pure* WM CBF (f_{WM}) contribution to that voxel. One can conceptually think of these *pure* tissue contributions as tissue-specific CBF density from which partial GM flow (f^p_{GM}) and partial WM flow (f^p_{WM}) can be subsequently computed from Eqs. [3] and [4]. Subjectwise averages of f^p_{GM} and f^p_{WM} are shown in Fig. 5, second and third rows, respectively; the net CBF is shown in the fourth row. Slices were chosen to represent the lower, middle, and upper parts of the brain. Corresponding images from PVE-uncorrected data are shown in the fifth row.

To get a sense of the voxelwise spatial distribution of the (f_{GM}/f_{WM}) ratio, the histogram of its subjectwise average values is shown in black in Fig. 6a; maps from a single subject are shown in Fig. 6b. The median and the mean (± SD) values of this ratio were ~3.2 and 3.4 (±0.4), respec-

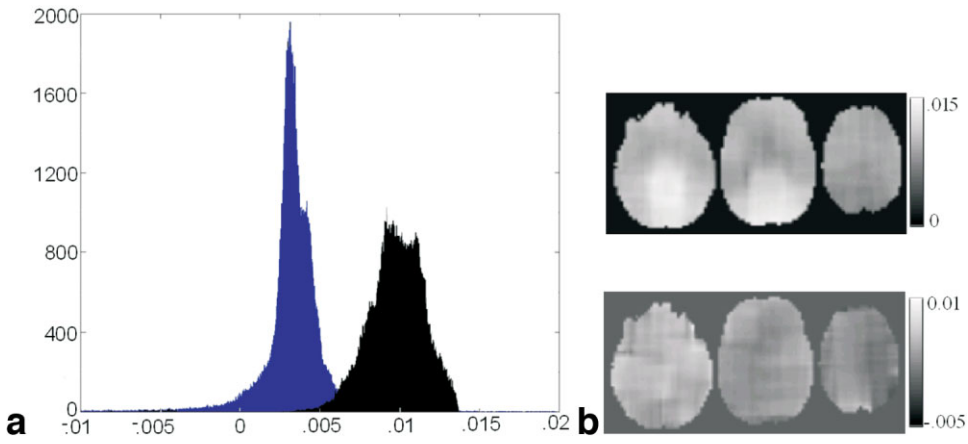

FIG. 2. **a:** Histograms of subjectwise averaged ASL signal images: $\delta m_{GM}/m_{GM}$ (black) and $\delta m_{WM}/m_{WM}$ (blue). **b:** Maps $\delta m_{GM}/m_{GM}$ (first row) and $\delta m_{WM}/m_{WM}$ (second row) from a single subject. Slices were chosen to represent the lower, middle, and upper parts of the brain. For all data, an 11 × 11 × 1 regression-kernel was used. [Color figure can be viewed in the online issue, which is available at www.interscience.wiley.com.]

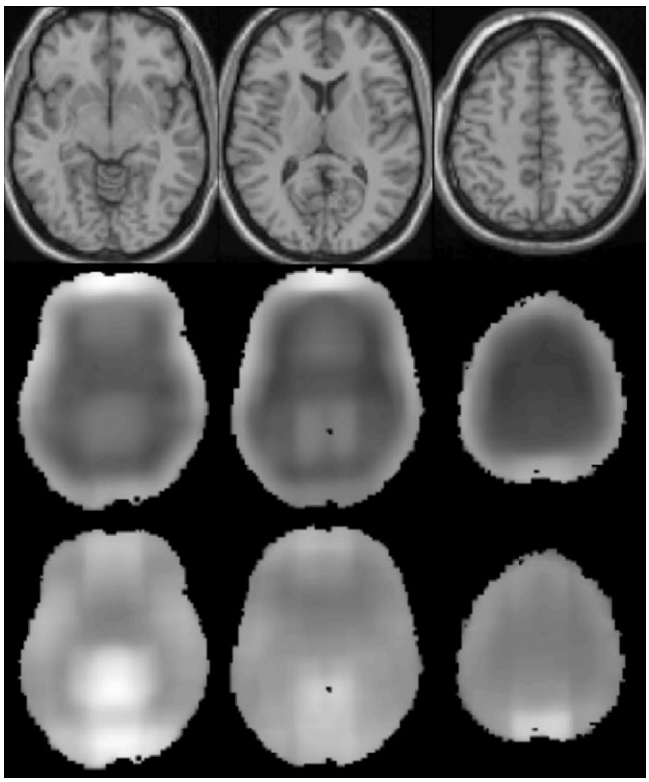

FIG. 3. Subjectwise averages of square root of MSE, ($\sqrt{MSE}$), of estimated EPI control (second row) and ASL difference (Δm) images (third row); SPGR of the corresponding slices are shown in the first row. Slices representing lower, middle, and upper parts of the brain are shown (corresponding MNI *z*-coordinates: 22, 30, and 49, left to right).

tively. The average (ratio) (f^p_{GM}/f^p_{WM}) was 5.8 ($\pm$ 0.8) reflecting, in addition to the flow difference, a difference in fractional volume between GM and WM.

Comparison With PVE-Uncorrected Baseline CBF Images

The PVE correction algorithm presented here calculates flow in a given tissue based on the raw ASL signal coming from that tissue alone, thus (theoretically) excluding any cross-contamination from the other tissues. In comparison, the uncorrected method is incapable of separating the individual tissue contributions. Consequently, the two methods should yield similar results in voxels with a high percentage of a given tissue while differing in the more mixed voxels. To test this prediction, we compared CBF values for pure GM CBF obtained from the PVE-corrected data with the CBF of PVE-uncorrected data from six ROIs with varying GM fractional volume: [0–0.2], [0.2–0.4], [0.4–0.6], [0.6–0.8], [0.8–1.0], and [0.95–1.0].

We made two predictions: 1) the value of the *pure* GM CBF should be independent of GM fractional volume because it is an implicit measure of the density of GM CBF, and as such, it should not depend on the voxel's GM "mass"; 2) the higher the GM fractional volume, the smaller the difference between the corrected and uncorrected methods. These predictions were borne out in Fig. 7. The first five ROIs were similar in size with an average number of voxels 46179 $\pm$ 9911; the sixth ROI was chosen as the ROI representing pure GM, and as such it was smaller (4549 $\pm$ 1080 voxels), which explains its higher SD in both methods (Fig. 7).

Comparison With PVE-Uncorrected Activation CBF Images

An application of most interest in ASL perfusion MRI is detection of regional changes in CBF due to activation. For one of the subjects, thresholded SPM{T} maps for the PVE-corrected activation signal, (Tap-Rest), for f^p_{GM}, [$T > 4.41$, $\alpha_{\text{corrected}} = 0.05$] and f_{NET} [$T > 4.41$, $\alpha_{\text{corrected}} = 0.05$], are shown overlaid on subject's SPGR in Fig.8a and 8b, respectively; no voxels survived the threshold for multiple comparisons for WM flow. The activation maps, [$T > 4.36$, $\alpha_{\text{corrected}} = 0.05$], for the conventional, PVE-uncorrected CBF images are shown in Fig. 8c. Data from the other subjects (not shown) were similar.

One can appreciate the additional information that can be obtained by separating the contribution of each tissue type in activation studies. For example, the number of voxels that showed a significant change in CBF due to activation was 41% $\pm$ 8% higher in f^p_{GM} than in the PVE-uncorrected images. We give a more quantitative treatment of the activation signal and its dependency on regression-kernel size in the following section.

"Smoothing" Effect of the Regression-Kernel and Its Dependence on Kernel Size

Clearly, the larger the regression-kernel, the more equations are available for regression analysis. The drawback is that the larger the regression-kernel size, the weaker is the assumption of uniformity of CBF values across the regression-kernel and the lower the effective spatial resolution of the CBF image. For the smallest regression kernel used ($5 \times 5 \times 1$), when compared with uncorrected, smoothed

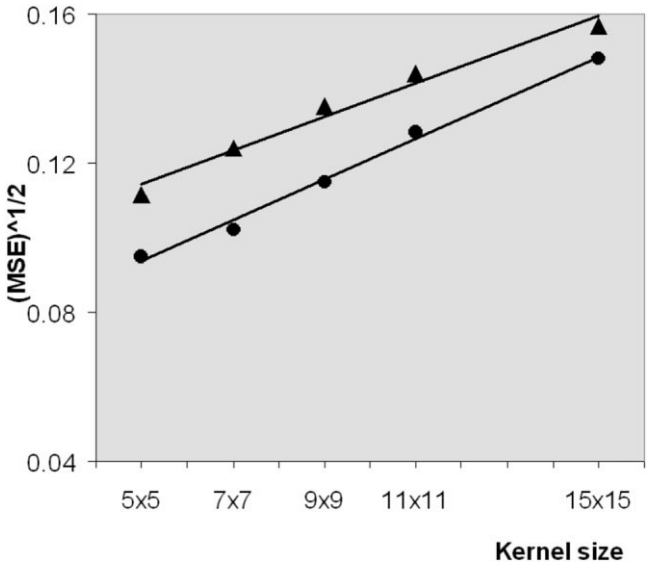

FIG. 4. Plots of the square root of MSE $\sqrt{MSE}$ vs. regression-kernel size for GM ($P[GM] > 0.8$) and WM ($P[WM] > 0.8$) are shown in circles and triangles, respectively. Note that solid lines are drawn to aid visual inspection.

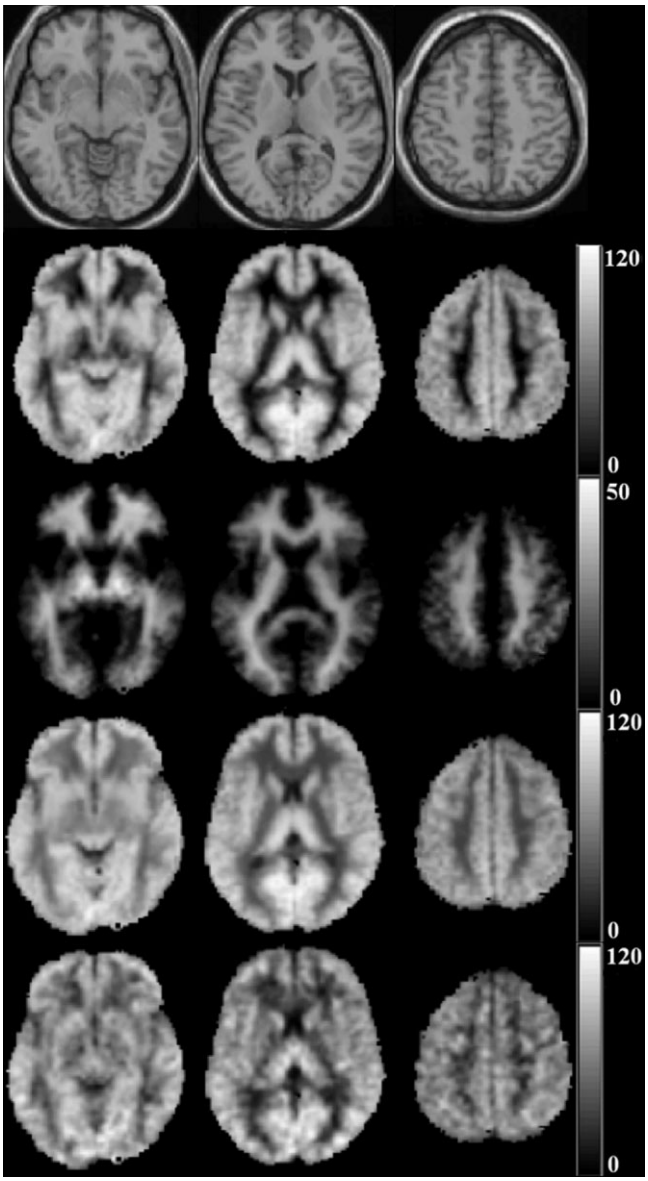

FIG. 5. Subjectwise average images of SPGR (first row); partial GM CBF, f^p_{GM}, (second row); partial WM CBF, f^p_{WM} (third row); net CBF image, $f^p_{GM} + f^p_{WM}$ (fourth row); and CBF images from PVE-uncorrected, unsmoothed data (fifth row). Slices representing the lower, middle, and upper parts of the brain are shown (MNI *z*-coordinates: 22, 30, and 49, left to right.)

data, the minimum difference (within ~1%) was found for the spatial smoothing filter of FWHH = 5 ± 2 mm. For the 15 × 15 regression-kernel, the largest kernel used, data were similar (within ~1%) to those smoothed with FWHH = 9 ± 4 mm.

Furthermore, we tested the dependence of the activation signal on the regression-kernel volume by comparing the activation data from regression-kernel sizes of 5 × 5 × 1, 7 × 7 × 1, 9 × 9 × 1, 11 × 11 × 1, and 15 × 15 × 1.

Figure 9 shows resting f_{GM} and activation f_{GM} for varying regression-kernel sizes in blue and purple, respectively. Data from the repeated experiment on this subject (2 months apart) are shown in dashed lines. In both cases, there was little variability in resting value f_{GM} with regression-kernel size supporting the assumption of local uniformity of resting f_{GM}. However, the activation CBF was higher for the smaller (5 × 5) regression-kernel size, implying a localized activation that is presumably spread out for larger regression-kernel sizes. Data from other subjects were similar in behavior; however, in one subject no voxels survived the threshold for multiple comparisons for regression-kernels 11 × 11 and 15 × 15.

Subjectwise averaged CBF values from 5 × 5 PVE-corrected data are compared with those from the PVE-uncorrected method in Fig. 10; the blue part of each column denotes the group-averaged resting value, while the purple section denotes the group-averaged CBF increase due to activation. As expected, both resting CBF (blue) and the activation-related CBF increase (purple) were larger in the PVE-corrected data.

DISCUSSION

We have developed a method that corrects for PVE in ASL MRI. Related algorithms have been shown to be effective in PET studies (5,6). The main difference between our algorithm and those developed for PET lies in the nonlinearity of these effects in ASL due to their presence in both the numerator and denominator of Eq. [2]. To circumvent the nonlinearity problem, we applied the regression analysis in EPI control images (to correct for PVE in the denominator of Eq. [2]) and the ASL difference images (correcting for PVE in the numerator of Eq. [2]).

The algorithm is based on posterior probability masks obtained from high-resolution SPGR images. However, the analysis is not dependent on the contrast used because only segmentation results (i.e., posterior probability values) and not actual image values are needed for analysis. Any high-resolution image that can be used for segmentation would work, independently of its contrast.

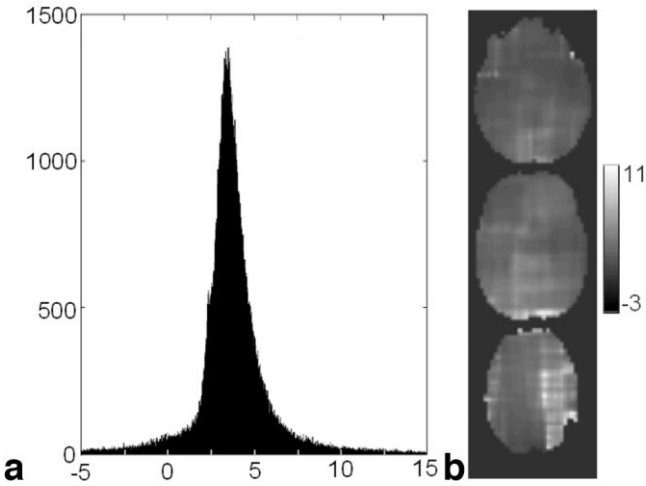

FIG. 6. **a:** Histogram of the subjectwise average ratio of GM-to-WM flow (f_{GM}/f_{WM}). The *y*-axis represent the number of voxels with a given GM-to-WM flow ratio. **b:** Maps of (f_{GM}/f_{WM}) from a single subject representing the lower, middle, and upper brain. An 11 × 11 × 1 kernel was used.

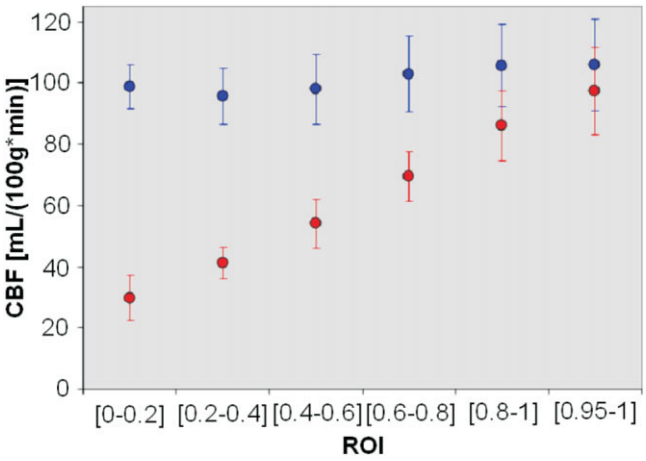

FIG. 7. Subjectwise averaged GM CBF values from ROIs varying in their GM content are shown in blue, whereas the respective net CBFs from the conventional, PVE-uncorrected, unsmoothed method are shown in red. Error bars represent ±1 SD. (Note the increase of SD values with the decrease in GM content for the PVE-corrected data.)

We compared data obtained using our algorithm against several a priori predictions based on theoretical considerations and results reported in literature for the tissue magnetization ratios as well as GM-to-WM flow ratios. Our algorithm yielded relative tissue intensities, $m_{CSF} : m_{GM} : m_{WM}$ of 1.6:1.2:1.0, in excellent agreement with theoretical predictions and experimental results from other studies (14,21).

ASL fractional signal images were obtained from estimation of tissue-specific magnetization and ASL difference images. The spread of the histogram for ASL signal in GM was larger than that in WM (Fig. 2), consistent with the idea that most of the intersubject variability in CBF comes from GM (11,13). Also, the histograms in Fig. 2 hint at multiple distributions within each tissue, which requires further investigation.

PVE-corrected ASL raw-signal images were used to obtain tissue-specific, *pure* CBF images and the voxelwise ratio of GM flow to WM flow was computed. This ratio in itself can be indicative of the severity of PVE. The reported values of this ratio range from [5.1–1.4] (2,9,13). The voxelwise range of ratios for our PVE-corrected data was [2.5–4.5] with an average of 3.4, in good agreement with high-resolution studies where PVE are expected to be minimal (1). Future work is needed to further investigate the spatial distribution and dependency of this ratio with age, gender, and other factors.

The results from PVE-corrected and PVE-uncorrected CBF values were very similar in homogenous GM voxels (Fig. 7) and ~20% higher in PVE-corrected images for voxels containing 80% or more GM. This result is relevant especially in studies of elderly subjects, where atrophy can be a factor in the CBF difference observed. For example, in a recent Alzheimer's disease (AD) ASL study, we found a depression of CBF in the AD group of ~42% as compared to age-matched controls; only voxels containing 80% or more GM were included in the analysis (22). It should now be possible to separate from that net effect the amount due to true physiological difference from that caused by PVE effects, which could be higher in the AD group due to possible thinning of GM with the disease (23,24). In another AD ASL study (9), the PVE were accounted for by assuming a fixed WM-to-GM flow ratio of 2.5, which, although reasonable, does not take into account any variability due to disease or intrasubject spatial variation.

A simple motor-task paradigm showed the utility of PVE correction algorithm in activation applications by detecting tissue-specific changes in CBF larger than those detected by the conventional, PVE-uncorrected method. Furthermore, to test the effect of regression-kernel size in activation signal, data were analyzed with regression-kernels of varying sizes. As expected, the baseline CBF values were independent of the regression-kernel size, agreeing well with the assumption of local uniformity in CBF. However, the activation CBF signal was highest for the smallest regression-kernel, implying a highly localized area of activation that could be diminished by using larger regression-kernels. In fact, in one of the subjects, the data for larger kernel sizes did not survive the threshold for multiple comparisons. Further investigation of the group sensitivity of the algorithm for activation studies is needed.

The regression error increased with kernel size (Fig. 4), presumably due to the weakening of the assumption of local uniformity for larger kernels. When selecting a kernel size, one should consider having it big enough to ensure that the analysis has the necessary equations to work with, but is not too big, since both the "blurring" effect and the fitting noise would be larger.

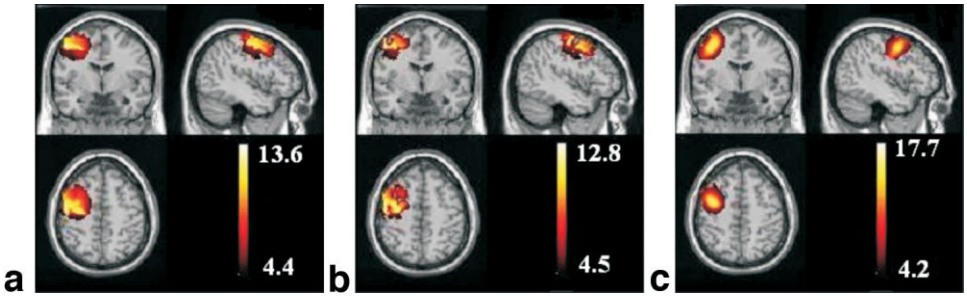

FIG. 8. SPM{T} maps (corrected for voxelwise multiple comparisons, $\alpha = 0.05$) of activation data from the subject's (**a**) partial GM CBF, (**b**) PVE-corrected net CBF, and (**c**) PVE-uncorrected net CBF (smoothed with a 12-mm Gaussian filter). Data shown are from the 11 × 11 × 1 kernel. Color bar represents the range of *t*-values above the threshold.

The algorithm has several drawbacks:

1. The employment of a regression-kernel causes an inherent "smoothing" of the data. The results shown here indicated that for 5 × 5 and 15 × 15 kernels, the "smoothing" effect was similar to that of a 5-mm and 9-mm Gaussian filter, respectively. It is important to emphasize that "smoothing" caused by the regression-kernel depends on the detailed structure of the local tissue fractions and therefore is different from a conventional spatial-smoothing filter. More in-depth work investigating the "blurring" effect of the regression-kernel is needed. This is especially relevant in studies of stroke and other ischemic lesions, where detection of small areas of CBF depression is important.

2. The algorithm requires tissue posterior probability images, preferably obtained from segmentation of a high-resolution structural image. This can be problematic for some cases involving elderly subjects, where WM hyperintensities may show up as GM and thus compromise tissue identification. Furthermore, in the presence of lesions, both the ability of good-quality segmentation and "blurring" caused by the regression-kernel could potentially compromise the performance of the algorithm. Masking out the lesion before running the analysis would help estimation in the surrounding voxels, but would not solve the problem of estimating CBF within the lesioned area itself.

3. Analysis for each time point (needed for activation studies) results in longer processing times. However, for baseline applications, processing times can be substantially shortened by using averaged images instead.

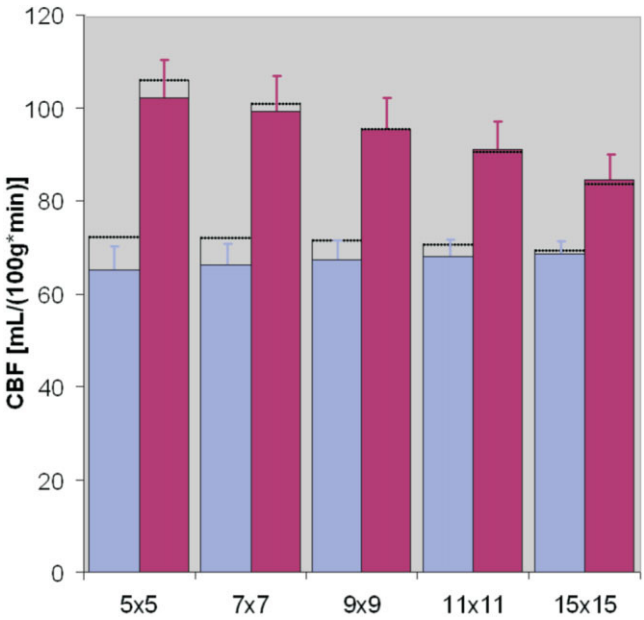

FIG. 9. Graph representing the dependency of the activation signal on kernel size. Columns in blue represent the baseline GM CBF values for each kernel size used; increase in CBF during activation is shown in purple. Data from the repeated experiment on this subject are shown in black dashed line. (Note the good replicability of the CBF measurement.) A conjunction SPM{T} mask was used in all cases (see Materials and Methods for details.) Error bars represent ±1 SD of temporal data for each condition. [Color figure can be viewed in the online issue, which is available at http://www.interscience.wiley.com.]

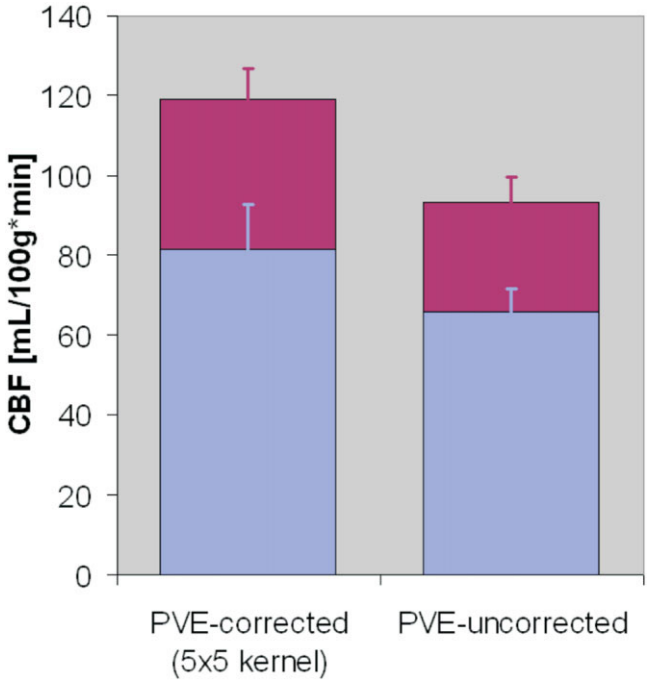

FIG. 10. Graphical comparison of PVE-corrected (with 5 × 5 × 1 kernel) vs. PVE-uncorrected activation data averaged across subjects. For better comparison, PVE-uncorrected images were smoothed with a 12-mm Gaussian filter. In both cases, baseline is shown in blue, while the amount of CBF difference due to activation is shown in purple. Error bars represent intersubject variability as +1 SD. [Color figure can be viewed in the online issue, which is available at http://www.interscience.wiley.com.]

CONCLUSIONS

We have implemented a method that corrects for PVE in CASL MRI. However, the method is not particular to CASL and it should be applicable to any implementation of ASL. We believe this method will be especially useful in age-related studies where PVE may be substantial due to brain atrophy.

AKNOWLEDGMENTS

The first author expresses her gratitude to Eric Zarahn, Ph.D, whose crucial input and invaluable expertise planted the seeds of this work.

REFERENCES

1. Donahue MJ, Lu H, Jones CK, Pekar JJ, van Zijl PC. An account of the discrepancy between MRI and PET cerebral blood flow measures. A high-field MRI investigation. NMR Biomed 2006;19:1043–1054.
2. Ye FQ, Berman KF, Ellmore T, Esposito G, van Horn JD, Yang Y, Duyn J, Smith AM, Frank JA, Weinberger DR, McLaughlin AC. H(2)(15)O PET validation of steady-state arterial spin tagging cerebral blood flow measurements in humans. Magn Reson Med 2000;44:450–456.
3. Du Y, Tsui BM, Frey EC. Partial volume effect compensation for quantitative brain SPECT imaging. IEEE Trans Med Imaging 2005;24:969–976.

4. Kops ER, Reilhac A. Correction of partial volume effects for PET imaging: a comparison study. IEEE 2004:4125–4129.
5. Schmidt K, Sokoloff L. A computationally efficient algorithm for determining regional cerebral blood flow in heterogeneous tissues by positron emission tomography. IEEE Trans Med Imaging 2001;20:618–632.
6. Aston JA, Cunningham VJ, Asselin MC, Hammers A, Evans AC, Gunn RN. Positron emission tomography partial volume correction: estimation and algorithms. J Cereb Blood Flow Metab 2002;22:1019–1034.
7. Alsop DC, Detre JA. Reduced transit-time sensitivity in noninvasive magnetic resonance imaging of human cerebral blood flow. J Cereb Blood Flow Metab 1996;16:1236–1249.
8. Golay X, Hendrikse J, Lim TC. Perfusion imaging using arterial spin labeling. Top Magn Reson Imaging 2004;15:10–27.
9. Johnson NA, Jahng GH, Weiner MW, Miller BL, Chui HC, Jagust WJ, Gorno-Tempini ML, Schuff N. Pattern of cerebral hypoperfusion in Alzheimer disease and mild cognitive impairment measured with arterial spin-labeling MR imaging: initial experience. Radiology 2005; 234:851–859.
10. Parkes LM. Quantification of cerebral perfusion using arterial spin labeling: two-compartment models. J Magn Reson Imaging 2005;22: 732–736.
11. Asllani I, Borogovac A, Wright C, Sacco R, Brown TR, Zarahn E. An investigation of statistical power for continuous arterial spin labeling imaging at 1.5 T. Neuroimage 2008;39:1246–1256.
12. Noth U, Meadows GE, Kotajima F, Deichmann R, Corfield DR, Turner R. Cerebral vascular response to hypercapnia: determination with perfusion MRI at 1.5 and 3.0 Tesla using a pulsed arterial spin labeling technique. J Magn Reson Imaging 2006;24:1229–1235.
13. Parkes LM, Rashid W, Chard DT, Tofts PS. Normal cerebral perfusion measurements using arterial spin labeling: reproducibility, stability, and age and gender effects. Magn Reson Med 2004;51:736–743.
14. Buxton R. Introduction to functional MRI. 1st ed. Cambridge: Cambridge University Press; 2002.
15. Kirk RG. Experimental design: procedures for the behavioral sciences. 3rd ed. Monterey, CA: Brooks/Cole; 1995. p 10.
16. Wang J, Alsop DC, Li L, Listerud J, Gonzalez-At JB, Schnall MD, Detre JA. Comparison of quantitative perfusion imaging using arterial spin labeling at 1.5 and 4.0 Tesla. Magn Reson Med 2002;48:242–254.
17. Herscovitch P, Raichle ME. What is the correct value for the brain–blood partition coefficient for water? J Cereb Blood Flow Metab 1985; 5:65–69.
18. Werner R, Norris DG, Alfke K, Mehdorn HM, Jansen O. Improving the amplitude-modulated control experiment for multislice continuous arterial spin labeling. Magn Reson Med 2005;53:1096–1102.
19. Aguirre GK, Detre JA, Zarahn E, Alsop DC. Experimental design and the relative sensitivity of BOLD and perfusion fMRI. Neuroimage 2002;15: 488–500.
20. Worsley KJ, Liao CH, Aston J, Petre V, Duncan GH, Morales F, Evans AC. A general statistical analysis for fMRI data. Neuroimage 2002;15: 1–15.
21. Zhou J, Golay X, van Zijl PC, Silvennoinen MJ, Kauppinen R, Pekar J, Kraut M. Inverse T(2) contrast at 1.5 Tesla between gray matter and white matter in the occipital lobe of normal adult human brain. Magn Reson Med 2001;46:401–406.
22. Asllani I, Habeck C, Scarmeas N, Borogovac A, Brown TR, Stern Y. Multivariate and univariate analysis of continuous arterial spin labeling perfusion MRI in Alzheimer's disease. J Cereb Blood Flow Metab 2008;28:725–736.
23. Gee J, Ding L, Xie Z, Lin M, DeVita C, Grossman M. Alzheimer's disease and frontotemporal dementia exhibit distinct atrophy-behavior correlates: a computer-assisted imaging study. Acad Radiol 2003;10: 1392–1401.
24. Swartz RH, Black SE, Sela G, Bronskill MJ. Cognitive impairment in dementia: correlations with atrophy and cerebrovascular disease quantified by magnetic resonance imaging. Brain Cognit 2002;49: 228–232.